Expulsion of runaway electrons using ECRH in the TCV tokamak

J. Decker, M. Hoppe, U.A. Sheikh, B.P. Duval, G. Papp, L. Simons, T. Wijkamp, J.A. Cazabonne, S. Coda, E. Devlaminck, et al.

OPEN ACCESS
IOP Publishing | International Atomic Energy Agency
Nuclear Fusion
Nucl. Fusion **64** (2024) 106027 (13pp)
https://doi.org/10.1088/1741-4326/ad6c61

Expulsion of runaway electrons using ECRH in the TCV tokamak

J. Decker[1,*], M. Hoppe[2], U. Sheikh[1], B.P. Duval[1], G. Papp[3], L. Simons[1], T. Wijkamp[4], J. Cazabonne[1], S. Coda[1], E. Devlaminck[1], O. Ficker[5], R. Hellinga[6], U. Kumar[1], Y. Savoye-Peysson[7], L. Porte[1], C. Reux[7], C. Sommariva[1], A. Tema Biwolé[1], B. Vincent[1], L. Votta[2], the TCV Team[a] and the EUROfusion Tokamak Exploitation Team[b]

[1] Swiss Plasma Center (SPC), Ecole Polytechnique Fédérale de Lausanne (EPFL), CH-1015 Lausanne, Switzerland
[2] Department of Electrical Engineering, KTH Royal Institute of Technology, Stockholm, Sweden
[3] Max Planck Institute for Plasma Physics, D-85748 Garching, Germany
[4] FOM Institute DIFFER 'Dutch Institute for Fundamental Energy Research', 5600 HH Eindhoven, Netherlands
[5] Institute of Plasma Physics of the CAS, CZ-18200 Praha 8, Czech Republic
[6] Department of Applied Physics and Science Education, Eindhoven University of Technology, Eindhoven 5600 MB, Netherlands
[7] CEA-IRFM, F-13108 Saint-Paul-les-Durance, France

E-mail: joan.decker@epfl.ch

Received 15 April 2024, revised 22 July 2024
Accepted for publication 7 August 2024
Published 30 August 2024

Abstract

Runaway electrons (REs) are a concern for tokamak fusion reactors from discharge startup to termination. A sudden localized loss of a multi-megaampere RE beam can inflict severe damage to the first wall. Should a disruption occur, the existence of a RE seed may play a significant role in the formation of a RE beam and the magnitude of its current. The application of central electron cyclotron resonance heating (ECRH) in the Tokamak à Configuration Variable (TCV) reduces an existing RE seed population by up to three orders of magnitude within only a few hundred milliseconds. Applying ECRH before a disruption can also prevent the formation of a post-disruption RE beam in TCV where it would otherwise be expected. The RE expulsion rate and consequent RE current reduction are found to increase with applied ECRH power. Whereas central ECRH is effective in expelling REs, off-axis ECRH has a comparatively limited effect. A simple 0-D model for the evolution of the RE population is presented that explains how the effective ECRH-induced RE expulsion results from the combined effects of increased electron temperature and enhanced RE transport.

[a] See Reimerdes *et al* 2022 (https://doi.org/10.1088/1741-4326/ac369b) for the TCV Team.
[b] See Joffrin *et al* 2024 (https://doi.org/10.1088/1741-4326/ad2be4) for the EUROfusion Tokamak Exploitation Team.
[*] Author to whom any correspondence should be addressed.

Keywords: runaway electron, ECRH, disruption

(Some figures may appear in colour only in the online journal)

1. Introduction

In tokamaks, runaway electrons (REs) can be generated when the toroidal electric field exceeds a critical value that is proportional to the plasma density [1]. In recent years, REs have been studied extensively as they present a threat for reactor-scale tokamaks where disruptions may generate multi-MA RE beams that could inflict significant damage to the first wall [2]. Strong RE populations have been observed in all phases of tokamak discharges : plasma startup, current rampup, full current regime, and post-disruption. In reactor-scale tokamak disruptions, RE generation is expected to be dominated by avalanches of knock-on collisions [3, 4], which depends critically upon the strength of a pre-disruption RE seed [5]. Tokamak operation can thus be made safer by supressing any RE seed before an eventual disruption, or by, at least, reducing the RE density.

The Tokamak à Configuration Variable (TCV) is equipped with diagnostics dedicated to fast electron physics and has developed scenarios with strong RE currents without significant danger to the machine vessel [6, 7]. With extensive real-time control including magnetic shaping, high power auxiliary heating and multiple gas injection systems, TCV has become particularly well suited to RE research [8]. In TCV, sustained RE beams are observed following disruptions induced by massive gas injection (MGI) only when a significant fraction of the plasma current is driven by REs before the disruption [6, 9].

REs are generated in a plasma with electron density n if the electric field E parallel to the magnetic field lines exceeds a critical value E_c beyond which the electric force overcomes the collisional friction force of electrons that are travelling close to the speed of light. Connor & Hastie expressed this critical field as [10]

$$E_c = \frac{ne^3 \ln\Lambda}{4\pi\varepsilon_0^2 mc^2}, \tag{1}$$

where $\ln\Lambda$ is the Coulomb logarithm, e the elementary charge, ε_0 the free space permittivity, m the electron rest mass and c the speed of light in vacuum. For $E > E_c$, electrons with sufficient momentum $p > p_c = mc(E/E_c - 1)^{-1/2}$ accelerate continually and are termed REs. REs can be generated by collisional diffusion through the $p = p_c$ boundary beyond which electrons undergo this net acceleration, referred to as the Dreicer mechanism [11]. In addition, a knock-on collision between an existing RE and a slower, free or bound, electron can result in both electrons now satisfying $p > p_c$, termed the avalanche process [3]. Experimentally, REs are detected only when $E \gg E_c$ [12]. By accounting for additional physical effects such as radiation losses, radial transport, and collisions with partially ionized impurities [13–16], an effective critical field larger than E_c can be defined to identify the conditions for RE generation [17, 18].

In TCV, an observable RE population is generated in plasmas where the density is sufficiently low such that the parallel electric field satisfies $E/E_c \gtrsim 10$ [8]. At sufficiently low plasma densities, strong RE growth is observed with the discharge entering a regime where a significant fraction of the toroidal plasma current is carried by REs. After an MGI-triggered disruption, a so-called "RE beam" carries the entire plasma current, as shown in section 2. Under otherwise identical conditions, applying ECRH before MGI results in a near-complete expulsion of the RE seed population preventing the formation of a RE beam following the triggered disruption. ECRH-induced RE expulsion is further characterised in section 3. The RE expulsion rate and the resulting RE current reduction are found to increase with ECRH power with estimations of RE loss rates and RE population reduction derived from experimental observations. A radial scan of ECRH power deposition shows that the RE population reduction is considerably stronger for centrally compared to off-axis deposited ECRH. A 0-D analysis of the ECRH expulsion dynamics is presented in section 4. The RE current decay during ECRH is associated with a transition from high to low RE current regime from the combined effect of higher RE losses and reduced avalanche RE generation due to the higher bulk electron temperature and correspondingly lower loop voltage. The paper concludes by discussing applications of the ECRH-induced RE expulsion and proposing scenarios to further characterise the underlying physical mechanisms.

2. Prevention of post-disruption RE beam formation using ECRH in TCV

TCV discharges presented in this paper feature a diverted, nearly circular, deuterium plasma with major radius $R = 0.89$ m, minor radius $a = 0.25$ m and a toroidal magnetic field on axis $B_T = 1.44$ T. From about $t = 0.1$ s onwards, the toroidal plasma current is maintained at $I_p = 120$ kA through feedback control of the central solenoid current. The presence of REs is monitored by PMTX, a photomultiplier tube sensitive to hard x-rays (HXRs) located outside the vessel. It is estimated that HXR photons with energies above 150 keV can traverse the TCV chamber and be detected by PMTX. Comparisons with dosimetry [19] show that, in the presence of significant RE populations, the PMTX signal remains approximately proportional to the HXR photon energy flux. The signal scales with RE energy and RE loss rate as HXR emission is dominated by RE-wall interaction in the absence of high-Z impurities within the plasma [9].

Studies of post-disruption RE beam generation in TCV concluded that a significant pre-MGI RE seed must exist for a RE

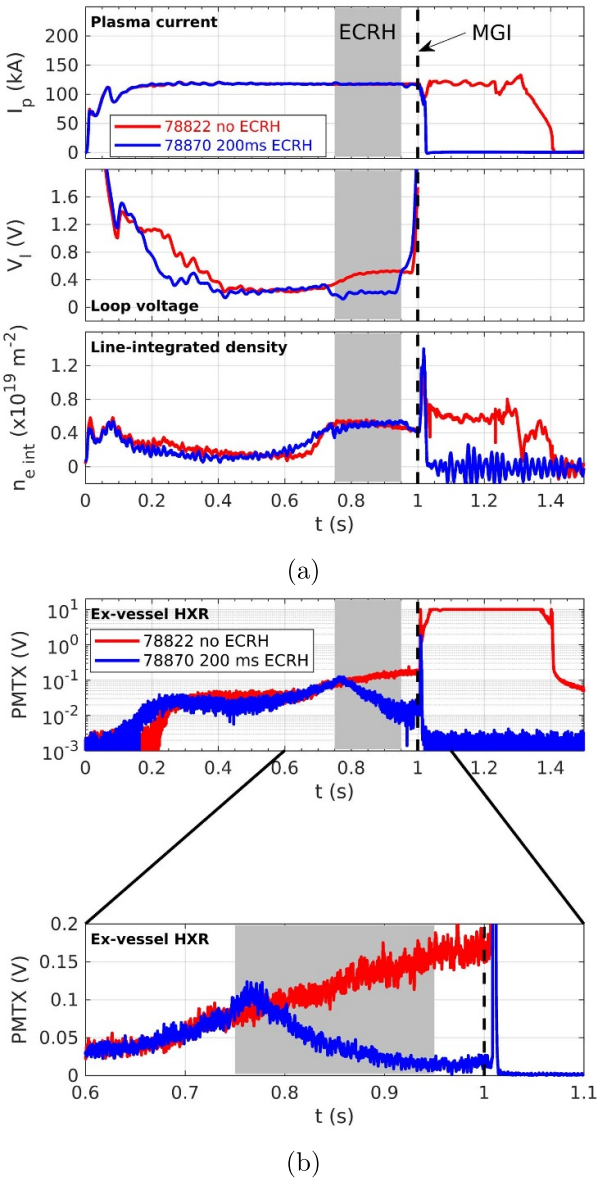

Figure 1. (*a*) Plasma current, loop voltage, line-integrated density; (*b*) raw signal from the PMTX diagnostic; as a function of time for TCV discharges #78822 (no ECRH) and #78870 (700 kW central ECRH between 0.75 and 0.95 s indicated by the grey area).

beam to form after a plasma discharge disruption trigerred by MGI [6]. In TCV discharge #78822 (figure 1), a strong RE seed is generated during an initial low density phase with a line integrated density $n_{\rm int} \leqslant 2\times10^{18}$ m^{-2} between $t=0.3$ s and 0.6 s. The HXR signal increases rapidly until it reaches a plateau between $t=0.4$ s and 0.6 s. As the HXR intensity rises, the loop voltage decreases from $V_{\rm loop}=1.2$ V to 0.3 V at $t=0.4$ s. As will be demonstrated in section 4, this decrease in loop voltage characterises a transition from a low to a high RE current regime, where ∼75% the plasma current is carried by REs.

In contrast with most TCV RE beam studies where the density is kept extremely low until MGI [6, 7], higher fueling is applied in this discharge from $t=0.6$ s onward. The density rises rapidly from $n_{\rm int}=1.5\times10^{18}$ m^{-2} at $t=0.6$ s to $n_{\rm int}=5.3\times10^{18}$ m^{-2} at $t=0.75$ s and is then held constant until MGI at $t=1.0$ s. This density increase is designed for RE dynamics comparison with discharge #78870 where ECRH power is applied and higher wall degassing inevitably increases the density. This nearly fourfold density increase leads to a remarkably modest reduction of the RE current, which still drives ∼50% of the plasma current at $t=0.75$ s, in accordance with an increase in the loop voltage to 0.6 V. The RE current remains relatively insensitive to density variations, a characteristic property of ohmic plasmas in the high RE current regime, as explained in section 4. The HXR signal does not decrease following this significant density increase but, instead, rises steadily. This suggests that the RE seed energy gain—as result of the higher loop voltage—more than compensates for the slightly reduced RE current. Massive injection of neon at $t=1.0$ s (7.2×10^{18} atoms) induces a plasma disruption. As indicated by the HXR signal saturating, a RE beam is formed, that now drives almost all the plasma current until the shot terminates at $t=1.4$ s. It is worth noting that, after a strong RE seed is established, raising the electron density by a factor 4 does not prevent the formation of a RE beam following the MGI-triggered disruption.

Figure 1 compares discharges #78822 and #78870, which are very similar until t = 0.75 s. In #78870 about 700 kW of ECRH power is applied between 0.75 and 0.95 s by an X-mode polarized EC wave power deposited on the high-field side (HFS) at $r/a=0.25$. With the toroidal magnetic field close to the maximum attainable at TCV, the ECRH power is deposited as centrally as possible for a 84 GHz microwave beam launched perpendicularly to the magnetic field. Upon ECRH application, the HXR signal increases sharply by ∼50% (figure 1(*b*)). This initial rise is followed by a steady decay of one order of magnitude over the 200 ms ECRH phase. Taking the HXR emission as proportional to the RE-wall collision frequency [9], the initial peak indicates a sudden increase in the RE loss rate upon ECRH onset, whereas the subsequent decay would result from a reduction in the RE current. The steady RE depletion is explained by an increased loss rate combined with a reduction in the RE avalanche gain as the loop voltage decreases during ECRH. At $t=1.0$ s, an MGI similar to that of #78822 also triggered a disruption, but was not followed by the formation of a RE beam. The application of ECRH thus prevented the formation of post-disruption RE beam by expelling the RE seed.

Lower energy REs are also monitored using the vertical electron cyclotron emission (VECE) diagnostic [20], figure 2. Radiation measured at frequencies 98.3 GHz and 108.8 GHz along a vertical line of sight intersecting the magnetic axis corresponds primarily to third harmonic ECE emission from electrons of energy $\mathcal{E}\simeq111$ keV and $\mathcal{E}\simeq51$ keV, respectively.[8] At

[8] Higher harmonic ECE emission by higher energy electrons may not be negligible. Estimating the importance of this contribution requires knowledge of the electron distribution function.

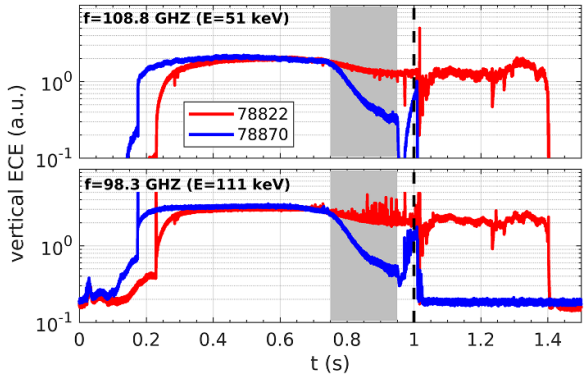

Figure 2. Uncalibrated vertical electron cyclotron emission at 108.8 and 98.3 GHz, as a function of time for TCV discharges #78822 (no ECRH) and #78870 (700 kW central ECRH between 0.75 and 0.95 s indicated by the grey area).

these frequencies the plasma is optically thin so VECE emission can be taken as proportional to the integrated density of REs at the corresponding energy along the vertical line of sight. VECE employs a viewing dump to avoid reflections, and the density is sufficiently low for lines of sight at the selected frequencies to originate from the dump. The effect of spurious reflections is thus neglected [21]. With a critical energy $\mathcal{E}_c \approx 50$ keV during the ECRH phase, the 108.8 GHz radiation is emitted by electrons near critical energy for which the electric and friction forces balance each other, whereas the 98.3 GHz radiation is emitted by REs.

In discharge #78822 without ECRH the VECE signals decrease by only 30% during the higher density phase between $t = 0.7$ s and 1.0 s. In contrast, VECE signals are found to decay strongly throughout the ECRH phase in TCV discharge #78870, indicating a depleting RE density at these energies. The absence of initial peak in VECE signals upon ECRH is expected as the radiation intensity depends on the integrated RE density along the line of sight that should not be increasing. Conversely, this observation reinforces the hypothesis that HXR emission, including the spike at ECRH onset, is proportional to the RE loss rate. The decay rate from the VECE signals across the first 100 ms in the ECRH phase is approximately 13 s^{-1}. It is independent of VECE frequency and nearly identical to that of the PMTX signal that monitors HXR emission from higher energy electrons impinging upon the wall.

3. Characterisation of ECRH-induced RE expulsion

3.1. Effect of ECRH injected power on RE dynamics

ECRH-induced RE expulsion is further probed by varying the applied ECRH power. Figure 3 shows the time evolution of a reference discharge without ECRH (#77318, similar to #77822). A significant RE population is generated during the

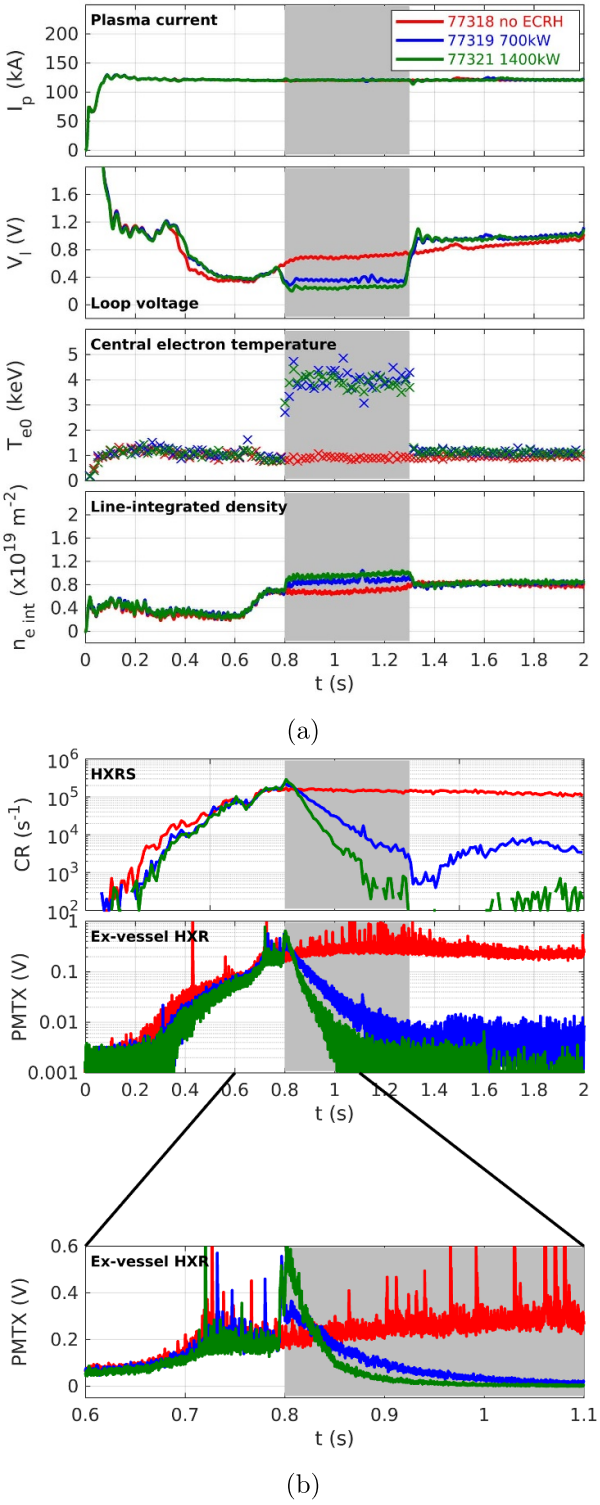

Figure 3. (*a*) plasma current, loop voltage, line-integrated density, and electron temperature; (*b*) count rate from the blind detector of the top vertical camera and raw signal from the PMTX diagnostic, as a function of time for TCV discharges #77318, #77319 and #77321 in which 0, 700 and 1400 kW of central ECRH is applied, respectively, between 0.8 and 1.3 s.

early, low density, phase. Around $t = 0.4$ s, the loop voltage decreases rapidly from $V_{\rm loop} = 1.2$ V to 0.4 V then remains relatively steady between $t = 0.45$ s and 0.65 s. In this high RE current regime, ∼70% of the plasma current is driven by REs, as estimated in section 4. For an RE dynamics comparison between discharges, with and without ECRH, the density is increased by ∼3× between $t = 0.6$ s and 0.7 s and then maintained.

Discharges #77319 and #77321 are identical to #77318 until $t = 0.8$ s, when 700 kW and 1400 kW of ECRH is applied, respectively, until $t = 1.3$ s. The 84 GHz, X-mode polarized EC wave is launched perpendicularly to the magnetic field and is deposited at $r/a = 0.25$ on the HFS.

In addition to the PMTX diagnostic, the evolution of the RE population is tracked by TCV's hard x-ray spectrometer (HXRS) that measures the count rate from the W-shielded blind[9] detector of the top HXRS camera [22], figure 3(*b*). It is estimated that only HXR photons with energy above 500 keV can traverse the W shielding of the camera and be registered. The HXR signals in the ECRH-free discharge #77318 are approximately constant after the density plateau is reached at 0.7 s. Similarly to #78870, the application of central ECRH in discharges #77319 and #77321 results in an initial peak in the HXR signals followed by a steady decay. Similar decay rates are measured in signals by the PMTX and HXRS diagnostics. The height of the initial HXR peak and the rate of the subsequent decay both increase with applied ECRH power, indicating a higher RE loss rate. In discharge #77319 (700 kW ECRH), the PMTX signal steadily decays during the ECRH phase, finally reaching two orders of magnitude below its peak value. In discharge #77321 (1400 kW ECRH), where the decay rate is higher, the PMTX signal decreases by three orders of magnitude from the peak value, attaining a steady state value from $t = 1.1$ s onwards.

3.2. Estimation of the RE loss rate and population reduction

HXR emission is monitored by PMTX, located outside the vessel, and by the HXRS camera array. It is estimated that, in the absence of heavy impurities, this HXR emission is dominated by RE-wall interaction, far exceeding the plasma bremsstrahlung emission [9], allowing the HXR intensity to be taken as proportional to the RE loss rate. This hypothesis is supported by the HXR intensity evolution during ECRH as RE-plasma bremsstrahlung cannot explain an initial peak followed by a steady decay. PMTX intensities are also found to be proportional to radiation dosimetric measurements from the LUPIN detector [19].

Assuming that HXR intensity increases with the energy of the RE impinging upon the wall and that RE losses are independent of RE energy, we can, to first approximation, consider that the HXR intensity Ψ be expressed by

$$\Psi = C\nu n_R K(\mathcal{E}) \tag{2}$$

[9] In each HXRS camera one detector referred to as the blind detector is shielded from the plasma by 2 cm of tungsten.

where ν is the RE loss rate, n_R the RE density, $K(\mathcal{E})$ is a monotonically increasing function of the average RE energy $\mathcal{E}$, and C is a time-independent constant that depends upon the RE-wall interaction physics, the diagnostic's characteristics and the plasma volume. The assumption that ν is indepentent of $\mathcal{E}$ is supported by the similar decay rates observed from VECE ($50 < \mathcal{E} < 110$ keV), PMTX ($\mathcal{E} > 150$ keV) and HXRS ($\mathcal{E} > 500$ keV) signals during the ECRH phase.

As seen in figure 3, at the onset of ECRH, the PMTX signal jumps, almost instantaneously, from $\Psi_0 = C\nu_0 n_{R0} K(\mathcal{E}_0)$ to a peak value $\Psi_1 = C\nu_1 n_{R1} K(\mathcal{E}_1)$. Assuming that the RE density $n_{R1} \simeq n_{R0}$ and energy $\mathcal{E}_1 \simeq \mathcal{E}_0$ have not changed significantly during this rapid transition, the relative increase in loss rate can be estimated from the initial HXR rise upon ECRH onset

$$\frac{\nu_1}{\nu_0} \simeq \frac{\Psi_1}{\Psi_0}. \tag{3}$$

From the PMTX signal in #77319 (700 kW) and #77321 (1400 kW) a relative peak height Ψ_1/Ψ_0—and thus a loss rate gain ν_1/ν_0 – of 2.0 and 3.0, respectively, are obtained.

After the initial peak, the HXR signal decreases until the end of the ECRH phase (#77319) or to a time-asymptotic limit (#77321). This is indicative of a decreasing RE density, confirmed by the absence of any significant RE current at the end of the ECRH phase where the loop voltage has now returned to its value before RE growth that is, itself, consistent with neoclassical conductivity calculations [23]. Defining $\Psi_2 = C\nu_2 n_{R2} K(\mathcal{E}_2)$ as the HXR signal intensity at the end of the ECRH phase, across which the loss rate $\nu_2 \simeq \nu_1$ is assumed to be constant, the ratio Ψ_2/Ψ_1 in HXR emission provides an estimate of the corresponding relative loss of REs

$$\frac{n_{R2}}{n_{R0}} \simeq \frac{\Psi_2/K(\mathcal{E}_2)}{\Psi_1/K(\mathcal{E}_0)}. \tag{4}$$

During the ECRH phase, the parallel electric field is strongly reduced but remains higher than the critical field ($E/E_c \gtrsim 3$). Assuming $\mathcal{E}_2 \approx \mathcal{E}_0$ we can take

$$\frac{n_{R2}}{n_{R0}} \approx \frac{\Psi_2}{\Psi_1} \tag{5}$$

with a value of $n_{R2}/n_{R0} \approx 10^{-2}$ for #77319 where the RE population was still decreasing when ECRH ceased, and $n_{R2}/n_{R0} \approx 10^{-3}$ for #77321 where Ψ_2 is taken as the asymptotic limit. A reduction of the RE density of three orders of magnitude is observed in TCV discharge #77321 until a steady-state is reached where residual RE generation balances RE losses.

As described in section 4, the HXR intensity evolution results from the competition between RE loss rate ν_1 and avalanche gain γ_{A1}. This can be estimated from the time evolution of Ψ in the early stage of the decay phase. We find $\nu_1 - \gamma_{A1} \simeq 16\ {\rm s}^{-1}$ for #77319 (700 kW) and $\nu_1 - \gamma_{A1} \simeq 31\ {\rm s}^{-1}$ for #77321 (1400 kW). The time evolution of the PMTX signal, figure 4, is compared to a model where $\Psi(t) = \Psi_0$ before ECRH ($t < 0.8$ s) and $\Psi(t) = \Psi_2 + (\Psi_1 - \Psi_2)\exp[-(\nu_1 - \gamma_{A1})t]$ during ECRH ($t > 0.8$ s).

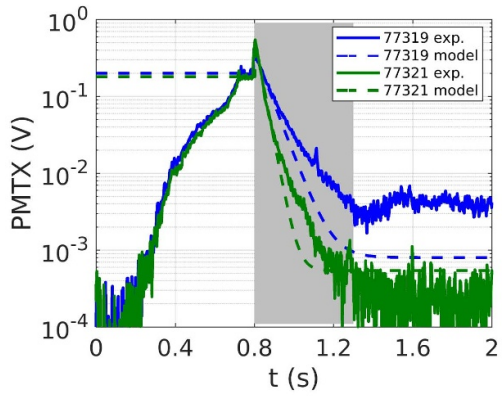

(a)

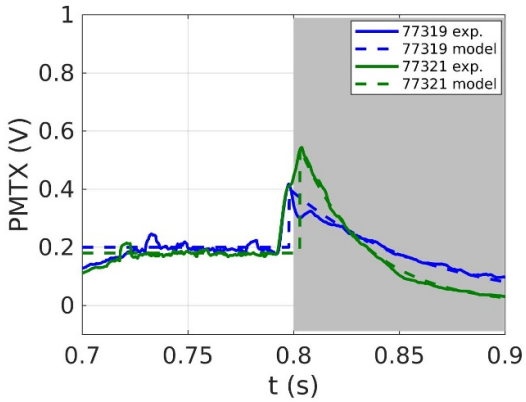

(b)

Figure 4. Measurement of the PMTX signal in TCV discharges #77319 (700 kW) and #77321 (1400 kW) compared to the model $\Psi(t)$.

In section 4, values of $\gamma_{A1} \simeq 7$ for #77319 and $\gamma_{A1} \simeq 4$ for #77321, respectively, are deduced during the ECRH phase. Combining equation (3) with ν_1 measurements provides an estimation for the RE loss rate, ν_0, before ECRH. For #77319 (700 kW), $\nu_1 \simeq 23$ s^{-1}, $\Psi_1/\Psi_0 \simeq 2.0$ and $\nu_0 \simeq 11$ s^{-1}. For #77321 (1400 kW), $\nu_1 \simeq 35$ s^{-1}, $\Psi_1/\Psi_0 \simeq 3.0$ and $\nu_0 \simeq 12$ s^{-1}. Reassuringly, highly similar pre-ECRH RE loss rates are derived from both discharges that were programmed identical until the ECRH phase. As shown in figure 3, more ECRH power significantly increases the RE loss rate. This increase, $\nu_1 - \nu_0$, is found proportional to the applied ECRH power and can be described by $(\nu_1 - \nu_0)/\nu_0 \simeq P/640$ kW.

3.3. Temperature profile and energy confinement time

The central electron temperature evolution measured by Thomson scattering (figure 3) is highly similar in discharges #77319 and #77321, from $T_{e0} \simeq 1$ keV before ECRH to $\simeq$ 3.5 keV during ECRH. The electron temperature profiles measured during the ECRH phases also overlap (figure 5),

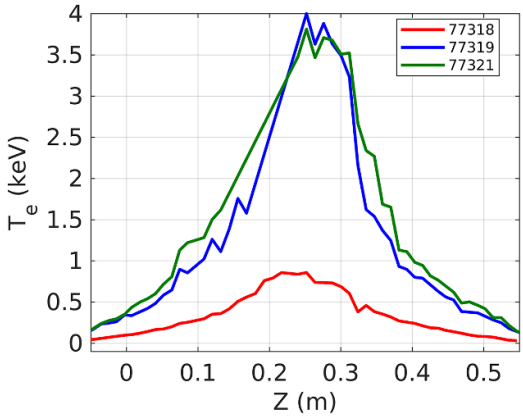

Figure 5. electron temperature profile from Thomson Scattering (TS) measurements averaged over the time range $t = [0.9, 1.1]$ s for TCV discharges #77318, #77319 and #77321 in which 0, 700 and 1400 kW of central ECRH is applied, respectively, between 0.8 s and 1.3 s. Profiles are plotted as a function of the respective vertical position Z where TS lines of sight insersect the vertical laser path.

suggesting that the plasmas are in a regime of saturated micro-turbulence with stiff electron temperature profiles where the transport is proportional to the input power [24, 25]. The energy confinement time, measured during the ECRH phase, correspondingly, decreases from $\tau_{E1} = 3.9$ ms in #77319 (700 kW ECRH) to $\tau_{E1} = 2.4$ ms in #77321 (1400 kW ECRH) to be compared to $\tau_{E0} = 9.5$ ms in the absence of ECRH (#77318). The reduction in energy confinement $\tau_{E1}^{-1} - \tau_{E0}^{-1} = 150$ s^{-1} for #77319 and $\tau_{E1}^{-1} - \tau_{E0}^{-1} = 310$ s^{-1} for #77321 is also found to be proportional to the applied ECRH power. ECRH-enhanced turbulent radial transport would thus be a possible mechanism to explain the corresponding increase in RE loss rate [26].

3.4. Effect of ECRH radial location on RE dynamics

In the TCV discharges presented so far, ECRH was launched perpendicularly to the magnetic field at a poloidal angle corresponding to EC power deposition close to the plasma centre. In a similar set of experiments, ~600 kW of ECRH (82.4 GHz, X-mode polarisation) was again launched perpendicularly where REs carried ~40% of the plasma current. The radial location of ECRH power deposition is varied between $r/a = 0.20$ (#76443) and $r/a = 0.45$ (#76444) by adjusting the EC poloidal launching angle, figure 6, with the resulting discharge time evolutions shown in figure 7. Whereas the radial location of power deposition has no significant effect on the plasma density, the increase in central plasma temperature due to ECRH is higher for central ECRH ($T_{e0} = 3$ keV) than off-axis ECRH (1.8 keV). The loop voltage required to drive the plasma current is higher in discharge #76444 ($V_{\text{loop}} = 0.4$ V) than in #76443 (0.3 V). The increase in loop voltage is, however, lower than that predicted by the effect of electron temperature on the plasma conductivity $\sigma \sim T_e^{3/2}$. Comparison with neoclassical conductivity model predictions [23] indicates that REs probably drive a significant proportion of the

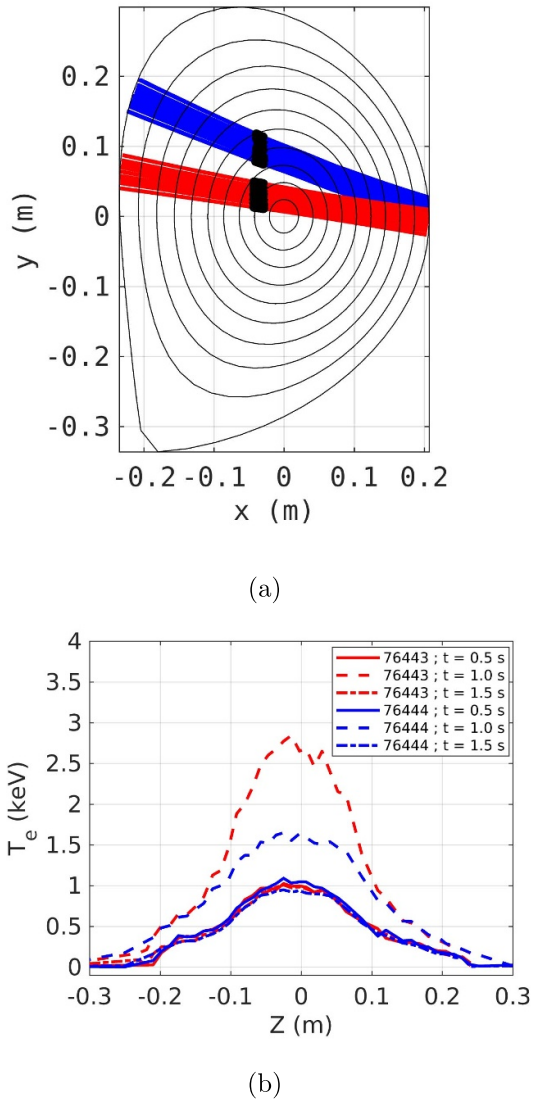

Figure 6. (*a*) ECRH propagation within a poloidal plane calculated by the RF propagation code C3PO [27] for TCV discharges #77443 (red) and #77444 (blue) where ECRH is applied between $t = 0.8$ and 1.3 s and deposited at radial locations $r/a = 0.25$ and $r/a = 0.45$, respectively; (*b*) correponding electron temperature profile from Thomson Scattering measurements averaged over the time range $t = [0.4, 0.6]$ s, $t = [0.9, 1.1]$ s, and $t = [1.4, 1.6]$ s.

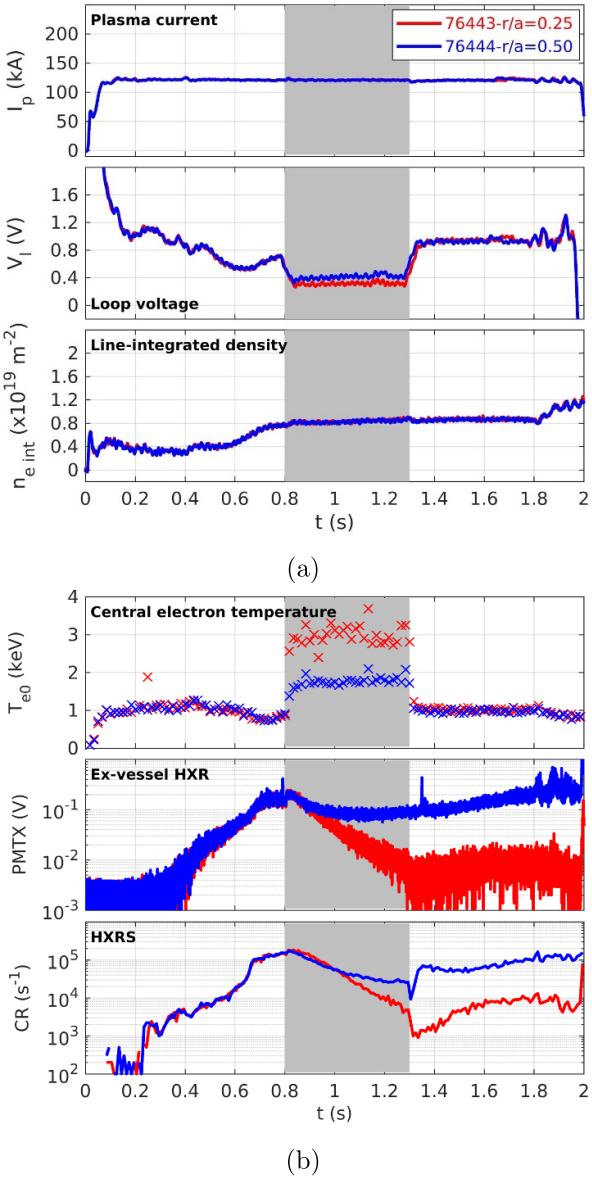

Figure 7. (*a*) Plasma current, loop voltage, line-integrated density; (*b*) central electron temperature; raw signal from the PMTX diagnostic, and count rate from the blind detector of the top vertical HXRS camera; as a function of time for TCV discharges #76443 and #76444 in which 700 kW of ECRH is deposited around $r/a = 0.2$ and $r/a = 0.45$, respectively, between 0.8 and 1.3 s.

plasma current during off-axis ECRH. This observation is confirmed by PMTX and HXRS signals that do not decay significantly in #76444. Although the RE loss rate increases upon off-axis ECRH, as identified by the initial PMTX peak, the slower decay and high asymptotic level of HXR signals indicate that the plasma remains in the high RE current regime described in section 4.

The relative height of the initial peak in PMTX signal is similar in #76443 and #76444. The corresponding estimate for the increase in RE loss rate (3) is $\nu_1/\nu_0 = \Psi_1/\Psi_0 \simeq 1.5$. The initial decay time is also similar, with $\nu - \gamma_{A1} \simeq 7\ \mathrm{s}^{-1}$. The HXR signal decays exponentially in discharge #76443 with a corresponding reduction of the RE density (5) of $n_{R2}/n_{R0} \approx 0.025$. For off-axis ECRH (#76444), however, the HXR intensity only decreases slightly before attaining a new steady-state with a modest RE density reduction $n_{R2}/n_{R0} \approx 0.5$ such that REs still drive $\sim$20% of the plasma current at the end of the ECRH phase. Interestingly, this contrasted evolution of the RE density for central vs off-axis ECRH is observed despite a similar RE loss rate.

4. A simple analytical model to describe ECRH-induced RE expulsion

4.1. High and low RE current regimes

It is shown in sections 2 and 3 that applying central ECRH in the presence of a significant RE population results in a strong reduction of the RE current by up to three orders of magnitude. ECRH-induced RE expulsion can be explained using a simple 0-D model that describes how the RE population evolves from a high RE current regime, characterised by a balance between RE losses and avalanche generation, to a low RE current regime where RE generation through the avalanche mechanism is negligible.

We assume a plasma with uniform electron density n, electron temperature T, current density J, and parallel electric field E. The evolution of the RE density n_R is taken to be

$$\frac{\mathrm{d}n_R}{\mathrm{d}t} = \Gamma - \nu n_R = \Gamma_D + (\gamma_A - \nu) n_R. \tag{6}$$

The RE generation rate $\Gamma = \Gamma_D + \gamma_A n_R$ includes a Dreicer generation rate Γ_D [11] and an avalanche growth rate γ_A that can be approximated by [3]

$$\gamma_A = \frac{\alpha e}{2mc \ln\Lambda} (E - E_c) \tag{7}$$

where α accounts for various effects such as magnetic trapping [28] that cannot be described ab-initio in a 0D model, and is considered here as a constant, to be determined. If $\gamma_A < \nu$ the RE density evolves towards a value $n_R = \Gamma_D/(\nu - \gamma_A)$. If $\gamma_A > \nu$ the RE density increases until some further saturation mechanism comes into play. Such a mechanism may include : (1) kinetic instabilities driven by increasing gradients in RE momentum space [29–31]; (2) momentum space vortices driven by radiation reaction forces [14, 32], possibly enhanced by resonant mechanisms [33–35]; (3) increased transport—and corresponding loss rate ν – resulting from changes in the plasma equilibrium due to the increasing RE-driven current; (4) reduced Ohmic field—with reduced avalanche gain γ_A—as a response of the plasma control system to the increasing RE-driven current [36].

The TCV plasmas discharges described in section 2 were under I_p-feedback control. The loop voltage evolution shows that, here, the RE saturation mechanism is provided by the Ohmic field reduction. We can model the plasma current density J as the sum of the thermal and RE contributions [36]. Approximating the parallel RE velocity to the speed of light

$$J = \sigma E + ecn_R \tag{8}$$

where σ is the plasma conductivity. We define $n_{Rp} \equiv J/(ec)$ as the density of REs required to drive all the plasma current. The RE density required to drive a current $I_p = 120$ kA in a circular uniform plasma with $a = 0.25$ m is $n_{Rp} = 1.3 \times 10^{16}$ m^{-3}, which is 2-3 orders of magnitude below the electron density of the discharges described in this paper. The control system uses feedback on the measured I_p to adjust the electric field

$$E = \frac{ec}{\sigma}(n_{Rp} - n_R) = \frac{J}{\sigma}\left(1 - \frac{n_R}{n_{Rp}}\right). \tag{9}$$

When the RE-driven current increases, the Ohmic drive is reduced and the avalanche growth rate decreases correspondingly from its maximum value $\gamma_{A\max} = \nu_A(1 - n/n_c)$ as

$$\gamma_A = \nu_A\left(1 - \frac{n}{n_c} - \frac{n_R}{n_{Rp}}\right) = \gamma_{A\max} - \nu_A \frac{n_R}{n_{Rp}} \tag{10}$$

where $\nu_A \equiv \alpha/(2\tau_c \ln\Lambda)$ is the maximum avalanche growth rate in the limit $n \to 0$, and n_c is the critical density below which REs can exist

$$n_c = \frac{4\pi\varepsilon_0^2 m^2 c^3}{\tau_c e^4 \ln\Lambda} \tag{11}$$

with $\tau_c = m\sigma/(e^2 n_{Rp})$ the corresponding relativistic collision time[10].

A homogeneous response of the electric field, as described by equation (9), is only applicable if the RE density evolves over time scales that are longer than the current redistribution time. Otherwise it is necessary to solve the induction equation as performed in codes such as GO [37] and DREAM [38]. Nonetheless, equation (10) can be combined with equation (6) to analyse steady-state plasma phases where the loop voltage is uniform and the RE-driven current is constant, i.e. $\mathrm{d}n_R/\mathrm{d}t = 0$:

$$\Gamma_D + \left[\gamma_{A\max} - \nu - \nu_A \frac{n_R}{n_{Rp}}\right] n_R = 0. \tag{12}$$

Solving equation (12) provides a solution for the steady-state RE density

$$n_R = \frac{1}{2}\left(n_{Rh} + \sqrt{n_{Rh}^2 - 4 n_{Rh} n_{Rl}}\right) \tag{13}$$

where we identify asymptotic expressions for high RE density

$$n_{Rh} \equiv n_{Rp}\nu_A^{-1}(\gamma_{A\max} - \nu) \tag{14}$$

and low RE density

$$n_{Rl} \equiv \frac{\Gamma_D}{\nu - \gamma_{A\max}}. \tag{15}$$

In TCV plasma conditions $\Gamma_D \ll \nu n_{Rp}$, indicating that the RE confinement time is too short for the Dreicer mechanism alone to sustain a significant RE current. Here, two clearly different regimes can be identified from equation (12):

[10] Here τ_c is defined as a function of the expected maximum electric field J/σ, in the absence of REs, and thus differs slightly from its usual expression $mc/(eE)$. The interpretation of n_c as a critical density remains since $n_R \to 0$ and $E \to J/\sigma$ when $n \to n_c$.

- a low RE current regime for $\gamma_{A\max} < \nu$ where the avalanche gain $\gamma_A \simeq \gamma_{A\max}$ cannot compensate RE losses and the steady-state RE density, $n_R \simeq n_{Rl} \ll n_{Rp}$, is proportional to the Dreicer generation rate and increases with the RE confinement time,
- a high RE current regime for $\gamma_{A\max} > \nu$ where the avalanche gain $\gamma_A \simeq \nu$ decreases from its maximum value $\gamma_{A\max}$ until it balances RE losses and the steady-state RE density is $n_R \simeq n_{Rh} \lesssim n_{Rp}$.

In the high RE current regime the RE density n_{Rh} can be rewritten as

$$n_{Rh} = \frac{1}{ec}\left[J - \sigma\left(E_c + E_\nu\right)\right] \tag{16}$$

where $E_\nu \equiv 2\alpha^{-1} mc \ln\Lambda\nu/e$ can be interpreted as a correction to the critical field accounting for RE transport and $E_c + E_\nu$ is now the effective critical field.

Exiting the high-RE current regime, or simply reducing n_{Rh}, can thus be achieved by one or more of the following : (a) a higher loss rate ν, (b) a higher electron temperature considering $\sigma \sim T^{3/2}$, (c) a higher density as $E_c \sim n$, (d) a lower plasma current as $J \sim I_p$. REs in TCV typically require $n/n_c = \sigma E_c/J < 10^{-1}$ so that, in the high RE current regime, density variations have a weak effect on n_{Rh} as observed experimentally in section 3.

Defining normalised quantities $\bar{n} \equiv n/n_c$, $\bar{\Gamma}_D \equiv \Gamma_D/(\nu_A n_{Rp})$, and $\bar{\nu} \equiv \nu/\nu_A$ we can express the normalised steady-state $\bar{n}_R \equiv n_R/n_{Rp}$ as

$$\bar{n}_R = \frac{1}{2}\left(\bar{n}_{Rh} + \sqrt{\bar{n}_{Rh}^2 + 4\bar{\Gamma}_D}\right) \tag{17}$$

where

$$\bar{n}_{Rh} = 1 - \bar{n} - \bar{\nu}. \tag{18}$$

REs can exist only if the density is sufficiently low so that $\bar{n} < 1$, and the high RE current regime requires a low RE loss rate $\bar{\nu} < 1 - \bar{n}$. When $\bar{\Gamma}_D \ll 1$, the high RE current regime results primarily from avalanche RE generation. The high and low RE current regimes are illustrated in figure 8 for parameters ($\bar{n} = 0.37, \bar{\Gamma}_D = 0.0024$) as a function of $\bar{\nu}$. We observe a sharp variation of the RE density around the transition $\nu = \gamma_{A\max}$ (or equivalently $\bar{n}_{Rh} = 0$) between the high and low RE current regimes, with n_R/n_{Rp} decreasing by two orders of magnitude for only a fourfold increase in $\bar{\nu}$. In comparison, increasing $\bar{\nu}$ while remaining within the high RE current regime does not affect the RE density significantly. In the low RE current regime, increasing $\bar{\nu}$ results in the RE density decreasing as $\bar{n}_R \sim 1/\bar{\nu}$.

4.2. Analysis of TCV #77321

The model developed in section 4.1 is applied here to TCV discharge #77321, described in section 3 and illustrated in figure 3, where five phases are identified where $V_{\rm loop}$ is approximately constant :

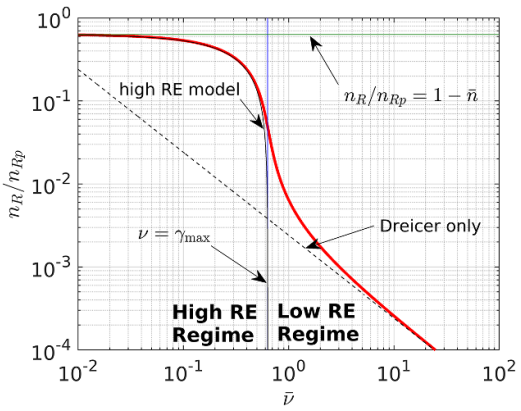

Figure 8. Normalized RE density n_R/n_{Rp} as a function of the normalized RE loss rate $\bar{\nu}$ for parameters $\bar{n} = 0.37$, $\bar{\Gamma}_D = 0.0024$. The asymptotic solutions $n_R = n_{Rh}$ and $n_R = n_{Rl}$ identified for the high and low RE regimes are indicated as dashed black lines. The transition $\nu = \gamma_{A\max}$ between the high and low RE regimes is marked as a blue vertical line.

(i) initial Ohmic plasma before RE growth (centered around $t = 0.25$ s),
(ii) lowest density, low loop voltage phase ($t = 0.55$ s),
(iii) higher density phase before ECRH ($t = 0.75$ s),
(iv) during ECRH after the RE decay phase ($t = 1.25$ s),
(v) after ECRH is turned off ($t = 1.50$ s).

In each phase, the measured density and loop voltage are used to estimate E/E_c by assuming a uniform loop voltage. The RE loss rates are obtained from the analysis of section 3 assuming – and verifying *a posteriori*—that $\nu \gg \gamma_A$ during ECRH. The main model parameters are listed in table 1.

The Dreicer generation rate during the ECRH phase, $\Gamma_D/n_{Rp} = 0.015\ \mathrm{s}^{-1}$, is derived from estimates of the steady-state RE density and the decay rate, equation (15). For comparison, a considerably higher estimate for the Dreicer RE generation rate during the initial, low-density, phase of the plasma discharge can be obtained from (6), see A, which yields $\Gamma_D/n_{Rp} \approx 0.2\ \mathrm{s}^{-1}$. The Dreicer growth rate is reduced by about an order of magnitude between the low density phase and ECRH phases. Furthermore, even in the absence of RE losses, driving a significant RE current through the Dreicer mechanism alone would take ∼5 s. With the loss rate, estimated at $\nu = 10\ \mathrm{s}^{-1}$, the asymptotic RE density would be limited to $n_R/n_{Rp} = \Gamma_D/(n_{Rp}\nu) \approx 0.02$. For low density Ohmic TCV plasmas in high RE current regime, RE generation is, thus, clearly dominated by the avalanche mechanism.

We can now describe the evolution of the RE population in discharge #77321 :

- In the initial low density phase $0.1 < t < 0.6$ s, $\nu < \gamma_{A\max}$, the RE growth rate is positive and the plasma evolves towards a high-RE current regime, indicated by the loop

Table 1. Parameters for plasma and RE dynamics corresponding to various time phases of TCV discharge #77321. The steady-state RE densities at $t = 0.55$ s and $t = 0.75$ s are calculated from I_p and $V_{\rm loop}$. An estimate for n_R/n_{Rp} after ECRH-induced RE expulsion can be derived from (5).

	t(s)	n_l ($\times 10^{19}$ m^{-3})	$V_{\rm loop}$ (V)	E/E_c	ν (s^{-1})	γ_A (s^{-1})	$\gamma_{A\,\max}$ (s^{-1})	n_{Rh}/n_{Rp}	Γ_D/n_{Rp} (s^{-1})	n_R/n_{Rp}
i)	0.25	0.8	1.00	27		25	25		0.2	
ii)	0.55	0.4	0.40	22	10	10	25	0.6		0.6
iii)	0.75	1.3	0.50	8	11	11	24	0.5		0.5
iv)	1.25	2.0	0.25	3	35	4	4	−4.8	0.015	0.0005
v)	1.50	1.5	1.00	15		24	24			

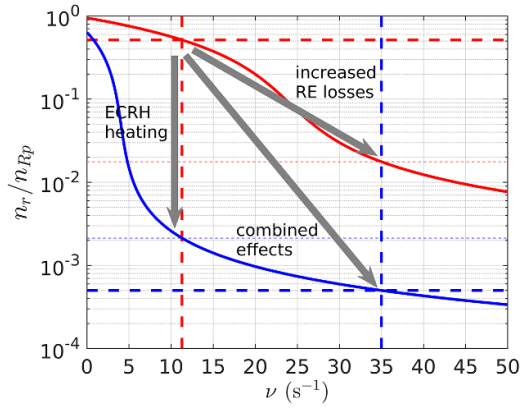

Figure 9. Normalized RE density n_R/n_{Rp} as a function of the normalized RE loss rate $\bar{\nu}$ for parameters corresponding to the pre-ECRH steady-state phase (red solid line, $\bar{n} = 0.06$, $\bar{\Gamma}_D = 0.0078$) and the ECRH phase (blue solid line, $\bar{n} = 0.37$, $\bar{\Gamma}_D = 0.0024$). The RE loss rates $\nu = 11$ s^{-1} and $\nu = 35$ s^{-1} measured respectively before and during ECRH are indicated along with the correponding n_R/n_{Rp}.

voltage decrease from $V_{\rm loop} = 1.0$ V to 0.4 V and an ensuing steady state $\nu = \gamma_A$ where avalanche generation compensates RE losses. This is a high RE current regime.

- From $t = 0.6$ s to $t = 0.7$ s the density increases from $n_{\rm int} = 2.5 \times 10^{18}$ m^{-2} to 7.0×10^{18} m^{-2} with a consequential increase in the critical field E_c. The loop voltage rises from $V_{\rm loop} = 0.4$ V to 0.5 V to maintain the avalanche growth rate $\gamma_A = \nu$. The plasma remains in a high-RE current regime.
- During the ECRH phase, the loss rate increases. In addition, ECRH heating increases the conductivity of thermal electrons and the control system reacts by reducing the loop voltage. The reduced avalanche RE generation can no longer compensate RE losses. The RE population decays to a balance between Dreicer generation and RE losses. The plasma is now in a low RE current regime.
- After ECRH, the loop voltage is higher than in the pre-ECRH phase. However, with a density now considerably higher than for the $t < 0.6$ s phase, Dreicer generation is comparatively low and RE regeneration over the remaining duration of the discharge can be neglected.

The transition from a high RE current regime before ECRH to a low RE current regime during ECRH is illustrated graphically for discharge #77321 by plotting the normalised RE density n_R/n_{Rp} as a function of the absolute RE loss rate ν (figure 9). We observe a three orders of magnitude decrease in the RE density from the combined effects of increased RE losses from $\nu = 11$ s^{-1} to 35 s^{-1} and the increased conductivity of thermal electrons attributed to ECRH (transition from the red to the blue curve).

We can infer that the heating effect of ECRH—and corresponding increase in conductivity—would have led to a RE density reduction by a factor ∼100 without an increase of the RE loss rate. Conversely, the increase in RE loss rate alone would have led to a RE density reduction by a factor ∼20. The combined effects induce a decrease of RE density by a factor ∼1000 as observed experimentally.

4.3. Analysis of ECRH phase in EC power and radial location scans

The model developed in section 4.1 is applied to the ECRH power and radial deposition scans by calculating n_{Rh} during the ECRH phase. Results are summarized in table 2. For TCV discharge #77319 (700 kW), illustrated in figure 3, it is found that $\nu = 23$ s^{-1} and $\gamma_{A\,\max} = 7$ s^{-1} – to compare with $\nu = 35$ s^{-1} and $\gamma_{A\,\max} = 4$ s^{-1} for TCV discharge #77321 (1400 kW). Despite a slightly higher loop voltage and a lower RE loss rate, the ECRH phase of #77319 is clearly in the low RE regime, indicated by the steady decay. A Dreicer rate similar to that of #77321 would indicate an asymptotic RE density of $n_R/n_{Rp} = 0.001$, which is compatible with experimental observations where the decaying RE density attained $n_R/n_{Rp} = 0.005$ at the end of the ECRH phase.

Table 2. Parameters for plasma and RE dynamics corresponding to the ECRH phase of discharges described in section 3. An approximate potential asymptotic post-expulsion RE density n_R/n_{Rp} is evaluated in shots #77319, #76443 and #76444 by using the value $\Gamma_D/n_{Rp} = 0.015\ \mathrm{s}^{-1}$ calculated in #77321.

shot #	P_{EC} (kW)	r/a	t (s)	n_l ($\times 10^{19}$ m^{-3})	V_{loop} (V)	E/E_c	ν (s^{-1})	γ_A (s^{-1})	$\gamma_{A\,\mathrm{max}}$ (s^{-1})	n_{Rh}/n_{Rp}	n_R/n_{Rp}
77 321	1400	0.25	1.25	2.0	0.25	3	35	4	4	−4.8	0.0005
77 319	700	0.25	1.25	1.8	0.35	4	23	7	7	−1.8	(0.001)
76 443	600	0.20	1.25	1.6	0.3	4	13	6	6	−0.9	(0.002)
76 444	600	0.45	1.25	1.6	0.45	6	16	9	9	−0.5	(0.003)

A similar observation can be made for shot #76443 (600 kW, $r/a = 0.20$), where the ECRH phase characterised by $\nu = 13\ \mathrm{s}^{-1}$ and $\gamma_{A\,\mathrm{max}} = 6\ \mathrm{s}^{-1}$ is also in the low RE current regime and the RE density measured at the end of the ECRH phase $n_R/n_{Rp} = 0.01$ is above the estimated asymptotic value $n_R/n_{Rp} = 0.002$.

In the case of off-axis ECRH in TCV, #76444 (600 kW, $r/a = 0.45$), this 0-D analysis yields $\nu = 16\ \mathrm{s}^{-1}$ and $\gamma_{A\,\mathrm{max}} = 9\ \mathrm{s}^{-1}$ again indicating a low RE current regime. The predicted asymptotic RE density $n_R/n_{Rp} = 0.003$ is two orders of magnitude below the estimated steady-state value $n_R/n_{Rp} = 0.2$ deduced from experimental measurements. The difference could indicate that the 0-D model is no longer applicable in the case of off-axis ECRH. A possible explanation is that off-axis ECRH increases the transport of REs located closer to the plasma edge but does not significantly affect core RE confinement.

5. Discussion and conclusions

REs are observed in TCV discharges when the parallel electric field exceeds the Connor-Hastie critical field by an order of magnitude or more. For very low density plasmas, the RE growth rates are sufficiently strong for REs to drive a significant fraction of the plasma current through an avalanche-dominated RE generation regime. The plasma current feedback system reacts to the increasing RE-driven current by reducing the parallel electric field until avalanche RE generation and RE losses balance. Here, the RE density is predicted to be resilient to density variations, as observed experimentally. Applying central ECRH to a TCV plasma in the high-RE current regime was seen to strongly reduce the RE density by up to three orders of magnitude. Such a reduction is sufficient to prevent the formation of a RE beam following a disruption triggered by massive gas injection. It is shown that the strongly reduced RE population is associated with a transition to a low-RE current regime where avalanche RE generation cannot compensate for RE losses. A 0D model, developed in section 4, demonstrates that this transition results from the combined effects of an increased RE loss rate and a reduced Ohmic electric field—with a correspondingly reduced RE avalanche generation rate—due to the increased conductivity of bulk electrons heated by ECRH. The RE decay rate and RE density reduction factor both increase with ECRH power. A radial scan of the ECRH deposition location showed that RE expulsion is much stronger for central than off-axis ECRH. A plausible explanation is that core RE confinement remains mostly unaffected by off-axis ECRH.

In a further set of experiments, not reported herein, varying the ECRH toroidal angle between discharges did not produce a noticeably different result. The HXR signal decay and asymptotic level are found to be similar for perpendicular ECRH, co, and counter-current drive configurations. It is worth noting that, under these conditions, the plasma current driven by EC waves was not significant and the loop voltage measured in the co- and counter-ECCD cases was near identical. It remains interesting to determine the effect of EC toroidal angle on RE expulsion in situations where the EC-driven current is significant. More generally, a strong reduction in the RE population resulting from a transition from a high- to low- RE density regime can be expected employing other sources of additional heating and current drive to reduce the Ohmic field, or by applying any method that augments RE losses.

An increased RE loss rate during ECRH is demonstrated experimentally but an underlying physics mechanism has not been identified. Resonant EC interaction is not expected between REs and EC waves and no significant MHD activity is observed during the ECRH phase. Kinetic instabilities may develop during ECRH in the presence of REs as observed for post-disruption RE beams in FTU [31]. The increased RE loss rate could alternatively be associated with an increase in microturbulence with ECRH power [26]. We observe that the electron temperature measured for 700 kW and 1400 kW of ECRH is nearly identical. This clear stiffness in the temperature profile suggests that turbulence driven radial energy transport increases with ECRH power. It is also plausible that RE transport increases with core turbulence as suggested by other fast electron experiments and simulations [39]. Future experiments are envisioned to characterise the effect of ECRH on turbulent transport to determine whether it can be more directly correlated with RE losses.

In a reactor-scale tokamak, RE generation during disruptions is expected to be dominated by the avalanche process, which depends upon the magnitude of the RE seed. ECRH-induced expulsion of any RE seed may be a path to prevent or limit RE beam formation should a disruption occur later in the discharge. Applying ECRH early in the discharge could reduce startup RE generation and prevent a possible transition to the dangerous slideaway regime. The simplified 0D model presented in this paper can be calibrated to track the

low and high RE regimes identified herein and provide a real-time control system where appropriate remedial action can be taken earlier and/or after a RE seed population has been formed.

In the TCV experiments described herein, RE expulsion during ECRH is particularly strong as the combination of increased RE transport and reduced avalanche RE generation is sufficient to initiate a transition from high- to low RE current regime, thereby decreasing the RE density by orders of magnitude. Additional work is required to determine the effect of ECRH on an existing RE seed for larger tokamaks.

Acknowledgments

The authors wish to thank A. Battey and H. Choudhury for insightful conversation on ECRH-induced RE expulsion mechanisms. This work has been carried out within the framework of the EUROfusion Consortium, partially funded by the European Union via the Euratom Research and Training Programme (Grant Agreement No 101052200—EUROfusion). The Swiss contribution to this work has been funded by the Swiss State Secretariat for Education, Research and Innovation (SERI). Views and opinions expressed are however those of the author(s) only and do not necessarily reflect those of the European Union, the European Commission or SERI. Neither the European Union nor the European Commission nor SERI can be held responsible for them.

Appendix. Estimation of the initial Dreicer RE generation

RE growth during the initial low density phase of discharges described in this paper is analysed by calculating the time-dependent RE density combining equations (6) and (10)

$$\frac{\mathrm{d}n_R}{\mathrm{d}t} = \Gamma_D + \gamma_{\mathrm{Ares}}\left[1 - \frac{n_R}{n_{Rh}}\right] n_R \tag{A.1}$$

where we define the resulting growth rate $\gamma_{\mathrm{Ares}} \equiv \gamma_{A\,\mathrm{max}} - \nu$ and the asymptotic high-RE solutions is $n_{Rh} = n_{Rp}\gamma_{\mathrm{Ares}}/\nu_A$. Starting from $n_R = 0$, the solution of equation (A.1) is approximately

$$\frac{n_R}{n_{Rh}} \simeq \Gamma_D \frac{1 - \exp\left[-\gamma_{\mathrm{Ares}} t\right]}{\Gamma_D + \gamma_{\mathrm{Ares}} n_{Rh} \exp\left[-\gamma_{\mathrm{Ares}} t\right]} \tag{A.2}$$

where we assume $\Gamma_D \ll \gamma_{\mathrm{Ares}} n_{Rh}$. We note that $n_R(0) = 0$ and $n_R(\infty) = n_{Rh}$. The corresponding time evolution is illustrated in figure A1 for parameters corresponding to the initial low density phase in TCV discharge #77321 described in section 3. An estimate for the Dreicer rate is obtained by measuring the elapsed time $t_{\mathrm{infl.}}$ to the inflexion point $\mathrm{d}^2 n_R/\mathrm{d}t^2 = 0$ for which

$$\Gamma_D = \gamma_{\mathrm{Ares}} n_{Rh} \exp\left[-\gamma_{\mathrm{Ares}} t_{\mathrm{infl.}}\right]. \tag{A.3}$$

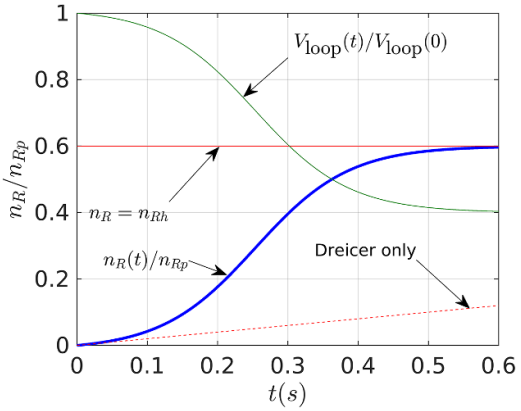

Figure A1. Time evolution of the normalized RE density n_R/n_{Rp} (solid blue line) for parameters corresponding to the initial low density phase of TCV discharge #77321 ($\Gamma_D/n_{Rp} = 0.2\ \mathrm{s}^{-1}$, $\gamma_{\mathrm{Ares}} \approx 15\ \mathrm{s}^{-1}$, $n_{Rh}/n_{Rp} = 0.6$). The solid red line indicates the time-asymptotic limit $n_R = n_{Rh}$ and the dashed red line shows the RE density evolution accounting only for Dreicer generation $n_R = \Gamma_D t$. The corresponding relative evolution of V_{loop} is also indicated (solid green line).

In the initial low density phase the inflexion point $t_{\mathrm{infl.}}$ can be estimated to be about 0.25 s. With $\gamma_{\mathrm{Ares}} \approx 15\ \mathrm{s}^{-1}$ and $n_{Rh}/n_{Rp} \approx 0.6$ we find

$$\frac{\Gamma_D}{n_{Rp}} \approx 0.2\ \mathrm{s}^{-1}. \tag{A.4}$$

ORCID iDs

J. Decker https://orcid.org/0000-0003-0220-2653
M. Hoppe https://orcid.org/0000-0003-3994-8977
U. Sheikh https://orcid.org/0000-0001-6207-2489
G. Papp https://orcid.org/0000-0003-0694-5446
T. Wijkamp https://orcid.org/0000-0003-3110-8682
J. Cazabonne https://orcid.org/0000-0001-7629-1375
S. Coda https://orcid.org/0000-0002-8010-4971
E. Devlaminck https://orcid.org/0000-0003-1185-8021
O. Ficker https://orcid.org/0000-0001-6418-9517
U. Kumar https://orcid.org/0000-0002-3258-8078
C. Reux https://orcid.org/0000-0002-5327-4326
A. Tema Biwolé https://orcid.org/0000-0002-4705-2743

References

[1] Breizman B.N., Aleynikov P., Hollmann E.M. and Lehnen M. 2019 Physics of runaway electrons in tokamaks *Nucl. Fusion* **59** 083001
[2] Lehnen M. *et al* 2015 Disruptions in ITER and strategies for their control and mitigation *J. Nucl. Mater.* **463** 39–48
[3] Rosenbluth M.N. and Putvinski S.V. 1997 Theory for avalanche of runaway electrons in tokamaks *Nucl. Fusion* **37** 1355
[4] Boozer. A.H. 2017 Runaway electrons and ITER *Nucl. Fusion* **57** 056018
[5] Hesslow L., Embréus O. Vallhagen O. and Fülöp T. 2019 Influence of massive material injection on avalanche

runaway generation during tokamak disruptions *Nucl. Fusion* **59** 084004
[6] Decker J. *et al* (the TCV Team and the EUROfusion MST1 Team) 2022 Full conversion from ohmic to runaway electron driven current via massive gas injection in the TCV tokamak *Nucl. Fusion* **62** 076038
[7] Sheikh U. *et al* (the ASDEX Upgrade Team, the TCV Team and the MST1 Team) 2024 Benign termination of runaway electron beams on ASDEX upgrade and TCV *Plasma Phys. Control. Fusion* **66** 035003
[8] Decker J. *et al* (the TCV Team and the EUROfusion Tokamak Exploitation Team) 2023 Recent progress in runaway electron research at TCV *2023 Proc. of the 29th IAEA Fusion Energy Conf.* (*London*, *16–21 October 2023*)
[9] Hoppe M. *et al* 2023 Runaway electron dynamics in the Tokamak à Configuration Variable *Proc. of the 49th EPS Conf. on Plasma Physics* (*Bordeaux, France*, *3–7 July 2023*)
[10] Connor J.W. and Hastie R.J. 1975 Relativistic limitations on runaway electrons *Nucl. Fusion* **15** 415
[11] Dreicer H. 1959 Electron and ion runaway in a fully ionized gas. I *Phys. Rev.* **115** 238–49
[12] Granetz R.S. *et al* 2014 An ITPA joint experiment to study runaway electron generation and suppressiona) *Phys. Plasmas* **21** 072506
[13] Aleynikov P. and Boris N.B. 2015 Theory of two threshold fields for relativistic runaway electrons *Phys. Rev. Lett.* **114** 155001
[14] Decker J., Hirvijoki E., Embreus O., Peysson Y., Stahl A., Pusztai I. and Fülöp T. 2016 Numerical characterization of bump formation in the runaway electron tail *Plasma Phys. Control. Fusion* **58** 025016
[15] Tinguely R.A., Granetz R.S., Hoppe M. and Embréus O. 2018 Measurements of runaway electron synchrotron spectra at high magnetic fields in Alcator C-mod *Nucl. Fusion* **58** 076019
[16] Hesslow L., Embréus O., Wilkie G.J., Papp G. and Fülöp T. 2018 Effect of partially ionized impurities and radiation on the effective critical electric field for runaway generation *Plasma Phys. Control. Fusion* **60** 074010
[17] Martín-Solís J.R., Sánchez R. and Esposito B. 2010 Experimental observation of increased threshold electric field for runaway generation due to synchrotron radiation losses in the FTU tokamak *Phys. Rev. Lett.* **105** 185002
[18] Stahl A., Hirvijoki E., Decker J., Embréus O. and Fülöp T. 2015 Effective critical electric field for runaway-electron generation *Phys. Rev. Lett.* **114** 115002
[19] Weisen H. *et al* 2024 TCV tokamak neutron shielding upgrade for dual NBI operation *Fusion Sci. Technol.* **80** 143–55
[20] Tema Biwole A., Porte L., Coda S. and Fasoli A. (TCV Team) 2023 Vertical electron cyclotron emission diagnostic on the Tokamak à Configuration Variable *Rev. Sci. Instrum.* **94** 103504
[21] Tema Biwole A., Porte L., Fasoli A., Simonetto A. and D'Arcangelo O. 2021 Performance of a high vacuum, high temperature compatible millimeter-range viewing dump for the vertical ECE experiment on TCV *Fusion Eng. Des.* **162** 112079
[22] Gnesin S. Coda S., Decker J. and Peysson Y. 2008 Suprathermal electron studies in the TCV tokamak: design of a tomographic hard-x-ray spectrometer *Rev. Sci. Instrum.* **79** 10F504
[23] Sauter O., Angioni C. and Lin-Liu Y.R. 1999 Neoclassical conductivity and bootstrap current formulas for general axisymmetric equilibria and arbitrary collisionality regime *Phys. Plasmas* **6** 2834–9
[24] Garbet X. *et al* (the JET EFDA Contributors) 2004 Physics of transport in tokamaks *Plasma Phys. Control. Fusion* **46** B557
[25] Garbet X. *et al* 2005 Profile stiffness and global confinement *Plasma Phys. Control. Fusion* **47** 957
[26] Hauff T. and Jenko F. 2009 Runaway electron transport via tokamak microturbulence *Phys. Plasmas* **16** 102308
[27] Peysson Y., Decker J. and Morini L. 2012 A versatile ray-tracing code for studying RF wave propagation in toroidal magnetized plasmas *Plasma Phys. Control. Fusion* **54** 045003
[28] Nilsson E., Decker J., Peysson Y., Granetz R.S., Saint-Laurent F. and Vlainic M. 2015 Kinetic modelling of runaway electron avalanches in tokamak plasmas *Plasma Phys. Control. Fusion* **57** 095006
[29] Pokol G., Fülöp T. and Lisak M. 2008 Quasi-linear analysis of whistler waves driven by relativistic runaway beams in tokamaks *Plasma Phys. Control. Fusion* **50** 045003
[30] Heidbrink W.W., Paz-Soldan C., Spong D.A., Du X.D., Thome K.E., Austin M.E., Lvovskiy A., Moyer R.A., Pinsker R.I. and Van Zeeland M.A. 2018 Low-frequency whistler waves in quiescent runaway electron plasmas *Plasma Phys. Control. Fusion* **61** 014007
[31] Carnevale D. *et al* (the FTU Team and the EUROfusion MST1 Team) 2021 Results on quiescent and post-disruption runaway electrons studies at frascati tokamak upgrade: RE mitigation via solid deuterium pellets and anomalous doppler instability *Nucl. Fusion* **61** 116050
[32] Andersson F., Helander P. and Eriksson L.-G. 2001 Damping of relativistic electron beams by synchrotron radiation *Phys. Plasmas* **8** 5221–9
[33] Hoppe M., Papp G., Wijkamp T., Perek A., Decker J., Duval B., Embreus O., Fülöp T. and Sheikh U.A. (the TCV Team and the EUROfusion MST1 Team) 2020 Runaway electron synchrotron radiation in a vertically translated plasma *Nucl. Fusion* **60** 094002
[34] Wijkamp T.A., Perek A., Decker J., Duval B., Hoppe M., Papp G., Sheikh U.A., Classen I.G.J. and Jaspers R.J.E. (the TCV Team and the EUROfusion MST1 Team) 2021 Tomographic reconstruction of the runaway distribution function in TCV using multispectral synchrotron images *Nucl. Fusion* **61** 046044
[35] Wijkamp T.A., Hoppe M., Decker J., Duval B.P., Perek A., Sheikh U., Classen I.G.J. and Jaspers R.J.E. (the TCV Team) 2023 Resonant interaction between runaway electrons and the toroidal magnetic field ripple in TCV *Nucl. Fusion* **64** 016021
[36] McDevitt C.J., Tang X.-Z., Fontes C.J., Sharma P. and Chung H.-K. 2023 The constraint of plasma power balance on runaway avoidance *Nucl. Fusion* **63** 024001
[37] Papp G. *et al* (JET EFDA Contributors) 2013 The effect of ITER-like wall on runaway electron generation in JET *Nucl. Fusion* **53** 123017
[38] Hoppe M., Embreus O. and Fülöp T. 2021 DREAM: a fluid-kinetic framework for tokamak disruption runaway electron simulations *Comput. Phys. Commun.* **268** 108098
[39] Cazabonne J. *et al* 2023 Experimental and numerical investigations of electron transport enhancement by electron-cyclotron plasma-wave interaction in tokamaks *Plasma Phys. Control. Fusion* **65** 104001